Available online at www.sciencedirect.com
ScienceDirect
Journal of Magnetic Resonance 182 (2006) 239–253
JMR Journal of Magnetic Resonance
www.elsevier.com/locate/jmr

Using a cross-coil to reduce RF heating by an order of magnitude in triple-resonance multinuclear MAS at high fields

F. David Doty [a,*], Jatin Kulkarni [a], Christopher Turner [b], George Entzminger [a], Anthony Bielecki [b]

[a] *Doty Scientific Inc., Columbia, SC, USA*
[b] *Francis Bitter Magnet Laboratory, Massachusetts Institute of Technology, MA, USA*

Received 5 February 2006; revised 13 June 2006
Available online 24 July 2006

Abstract

Four different coil designs for use with MAS in triple-resonance multi-nuclear experiments at high fields are compared, using a combination of finite element analysis (FEA) software and NMR experiments, with respect to RF field strength per unit power and relative sample heating, as governed by mean E/B_1 within the sample region. A commercial FEA package, Microwave Studio 5.1 by Computer Simulation Technology (CST) is shown to obtain remarkably accurate agreement with the experiments in Q_L, L, B, E, and mode frequencies in all cases. A simplified treatment of RF heating in NMR MAS samples is derived and shown to agree with the NMR experimental results within about 10% for two representative stator designs. The coil types studied include: (1) a variable-pitch solenoid outside a ceramic coilform, (2) a conventional solenoid very closely spaced to the MAS rotor, (3) a scroll coil, and (4) a segmented saddle cross coil (XC) for ^{1}H with an additional solenoid over it for the two lower-frequency channels. The XC/solenoid is shown to offer substantial advantages in reduced decoupler heating, improved S/N, and improved compatibility with multinuclear tuning and high-power decoupling. This seems largely because the division of labor between two orthogonal coils allows them each, and their associated circuitry, to be separately optimized for their respective regimes.

Keywords: MAS; RF heating; Cross-coil; Electric fields; Homogeneity; Probe

1. Introduction

While MRI RF coil analyses have often carefully calculated sample losses, most prior published analyses of small coils for solids NMR have largely ignored the sample loss. This has often been acceptable at low fields. However, when conventional solenoids are used in high-field solids NMR MAS spectroscopy of biological samples, RF decoupler heating has frequently imposed significant limitations on line narrowing. Although decoupling RF field strengths above 100 kHz have been demonstrated above 700 MHz in triple resonance probes [1], common approaches require either very small samples (~10 μL) or very low duty cycles to prevent damage to biological samples from severe RF heating. Neither of these approaches is always satisfactory, as they compromise S/N. An important objective in NMR coil design at high fields becomes minimizing the ratio E/B within the sample, as the E field gives rise to the sample heating, but the NMR sensitivity is proportional to efficiency of producing the B field.

In this study, we compare in some detail several different coil/stator designs for use with 4 mm rotors (sample volume up to 70 μL) in triple-resonance multi-nuclear experiments at 750 MHz. The coil designs include: (1) a variable-pitch solenoid outside a ceramic coilform, (2) a constant-pitch solenoid very closely spaced to the MAS rotor, (3) a scroll coil, and (4) an optimized segmented saddle coil—identified as the Cross Coil (XC)—for ^{1}H with an additional solenoid over it for the two lower frequency channels.

* Corresponding author. Fax: +1 803 736 5495.
E-mail address: david@dotynmr.com (F.D. Doty).

1090-7807/$ - see front matter © 2006 Elsevier Inc. All rights reserved.
doi:10.1016/j.jmr.2006.06.031

The optimized XC is similar to an earlier version which began from a derivative of the Alderman-Grant coil [2]. The preliminary XC was developed using in-house software based primarily on quasi-static **A** and **B** field calculations along with simple sample and conductor loss models [3]. Fortunately, full-wave electromagnetic software has recently become commercially available that is now capable of accurately and efficiently handling all aspects of the complex NMR coil problem, including losses in thin metal conductor sheets, sample losses, radiation, and lumped elements. The more completely optimized XC/solenoid gives improved B_1 homogeneity and S/N on all channels, and we now have a much improved picture of the RF heating problem.

The peak (central) RF sample heating by the optimized XC was found to be lower by a factor of 10–30 compared to that of the 4 mm solenoids. Also, the B_1 homogeneity, S/N, and peak B_1 capability for the XC were found to be significantly better than for the solenoids, especially for lossy dielectric samples. While the advantages of the XC/solenoid are less for smaller rotors and lower fields, its reduced heating of lossy samples is still significant even for 2.5 mm rotors at 700 MHz and quite substantial at higher frequencies.

We also look briefly at several circuits suitable for triple-resonance at high fields and show that the use of an XC for ^{1}H, with the low frequency (LF) and mid-frequency (MF) on a magnetically orthogonal solenoid, permits substantial simplifications in triple-resonance multinuclear circuits.

2. Theory

2.1. Sample power absorption

The power loss P_S in a sample may be calculated by either of the following equivalent expressions:

$$P_S = \frac{1}{2}\int \sigma E^2 \, dV \tag{1}$$

$$P_S = \frac{\omega}{2}\int \varepsilon_0 \, \varepsilon'' E^2 \, dV \tag{2}$$

where σ is the electrical conductivity, $\boldsymbol{E}$ is the electric field, ω is the angular frequency, ε_0 is the permittivity of free space, $\varepsilon'' = \varepsilon_r \tan\delta$, where ε_r is the relative permittivity and $\tan\delta$ is the loss tangent, and dV is a volume element. For 45 mM saline at 750 MHz, $\sigma = 0.5$ S/m, $\varepsilon_r = 76$, and $\tan\delta = 0.34$ at 310 K. The first expression is more often used, primarily because the conductivity of ionic conductors has little frequency dependence. In either case, one must determine **E**.

The **E** field satisfies the following:

$$E = -\partial A/\partial t - \nabla \Phi_E \tag{3}$$

where **A** is the magnetic potential vector field and Φ_E is the scalar electric potential due to electric charges. While quasi-static calculations of the **A** vector are straightforward for a known current distribution, the conservative **E** field arising from the second term in Eq. (3) is generally intractable analytically, except perhaps in some extremely simple cases. It often comes as a surprise that for multi-turn solenoids the second term in Eq. (3) may be an order of magnitude larger than the first term throughout the sample; and, unlike **A**, its direction is seldom perpendicular to **B**. Hence, the quasi-static calculation of **A** is of little value in itself. The only practical approaches to determining power absorption are either to utilize well-validated full-wave 3D EM software or to perform careful experiments.

The power absorbed by the sample may be determined from measurement of the isolated unloaded and loaded Q's of the tuned coil. (Recall the isolated Q is twice the matched Q, Q_L, the value more commonly reported outside the NMR literature.) The measured isolated Q_0 (coil and capacitors) and *isolated* total Q_T (coil, capacitors, and sample) allow calculation of a sample Q_S from the following relationship:

$$\frac{1}{Q_T} = \frac{1}{Q_0} + \frac{1}{Q_S} \tag{4}$$

The power absorbed by the sample for the matched, loaded coil is then

$$P_S = P_i Q_T / Q_S \tag{5}$$

where P_i is the incident power. In fact, this has been the primary method of accurately determining absorbed power in complex NMR coils until quite recently. We find that Q_T/Q_S is about 0.7 for 60 μL, 100 mM saline samples at 750 MHz inside single-tuned four-turn solenoids. For the XC, on the other hand, this ratio is about 0.4, and Q_T is three times that for the solenoid. Note that Q_S here is much larger than the value given by Tropp [4], $(\tan\delta)^{-1}$, as the electric energy here within the sample is but a small fraction of the total electric energy.

2.2. Finite element analysis software

In late 2002, we carried out rather extensive evaluations of three leading "full-wave 3D EM" packages and concluded that for RF coil problems similar to those in this study, Microwave Studio (MWS) 4.3 by Computer Simulation Technology (CST) was significantly better suited and more accurate than the other software we evaluated, HFSS by Ansoft, and XFDTD by REMCOM. Subsequently, we also confirmed the later release MWS 5.0.2 to consistently agree within our experimental accuracy, generally within 1–3% on mode frequencies, for a wide range of NMR and MRI RF coil problems, including small solenoids and cross coils as presented shortly, and larger cases in which the conditions were near dielectric resonance within the sample.

This CST code is based on a discretized solution of the integral formulation of Maxwell's equations; hence, the method is referred to as finite integration technique (FIT) [5]. To solve these equations, a finite calculation domain

is defined enclosing the application problem. A structured Cartesian mesh is created for half of the field equations (**E** and **B**), and a second Cartesian mesh, offset by half the element size in each direction from the first mesh, is created for the other half of the field equations (**H** and **D**). The use of two, offset meshes in this way reduces discretization errors. Obtaining accurate solutions with reasonable mesh sizes requires careful handling of mesh elements containing several different materials, especially when one material is a lossy metal and another material is a normal dielectric. CST has devoted considerable effort to optimizing the calculation of the mean effective fields and losses within these troublesome cells. The result is often a considerable improvement in the accuracy (compared to classical staircase boundary approximations) in the calculation of losses and modes for structures containing complex, intricate features. The mode frequencies are usually calculated within 2% of the experimental values (even for double resonance coils), and the calculated B_1 magnitude usually agrees within 5% with the NMR experiments for the types of coils presented shortly.

The discretized mesh equations can be solved either in the time domain by a transient finite difference time domain (FDTD) approach, or in the frequency domain using second-order harmonic relations. In all our cases, we have used the transient method, primarily because it provides a broad spectrum solution but also because the frequency domain solver was known to have quite a number of bugs until quite recently. An auto-recursive filter may be applied to the time-domain response, which often allows an order-of-magnitude reduction in the computational time required to obtain accurate mode frequencies; but for high absolute accuracy in the fields, impedance, S11, and VSWR plots from a transient excitation, the simulation must run until the energy has largely decayed, and this can take quite a long time. For example, version 5.0.2 has taken 20–50 h on a 3 GHz single-processor P4 for some of our unloaded XC/solenoid cases shown shortly. We note, however, that some MRI RF coil problems run in a few hours, and many common microwave problems run in a few minutes. The eigenmode solver is several orders of magnitude faster, but it does not handle lumped elements nor does it handle losses well.

2.3. The fields of the RF solenoid at high frequencies

Although the solenoid has been widely used for solids NMR for five decades, the detailed characteristics of its fields are not widely appreciated, especially at high frequencies. Hence, we first take a close look at the RF solenoid with 4 mm rotors at 750 MHz.

The first coil geometry, as shown in Fig. 1, is a four-turn solenoid wrapped over the central portion of a ceramic MAS stator having a central outside diameter (OD) of 5.1 mm. The coil wire is of oval cross-section, as shown more clearly in the *H*-vector plot (recall, $\mathbf{B} = \mu_0\mathbf{H}$) of Fig. 2 in the *XZ* plane. (We denote the axis of the spinner as the *z*-axis in all MAS coil coordinate systems.) The solenoid is edge wound with the wire's major axis in the radial direction, as this allows an orthogonal cross coil, presented shortly, to perform much better with minimal loss in performance of the solenoid.) The sample, with $\sigma = 0.5$ S/m and $\varepsilon_r = 80$ (corresponding approximately to 45 mM saline at 750 MHz, 293 K), is a cylinder of 3 mm diameter and 8 mm length inside a zirconia rotor ($\varepsilon_r = 26$) of 4 mm OD, and the MAS stator is of Si_3N_4 ($\varepsilon_r = 7$). The overall (outside) axial length of the solenoid is 8.2 mm, and the pitch is increased near the center to improve B_1 homogeneity. The coil is balanced, tuned, and matched with ATC-100B chip capacitors of appropriate values for 750 MHz (0.5 pF balance, 0.5 pF match, and 0.13 pF tune). The capacitor *Q* values were calculated from the following empirical expression

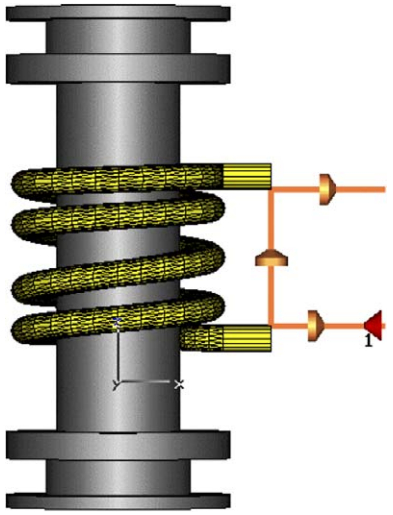

Fig. 1. Coil #1, the 4-turn solenoid outside the ceramic MAS stator. Lumped elements, in this case capacitors, are depicted in CST MWS as chamfered discs. The rings at the ends of the stator form the sides of the manifold channels for the radial air-bearing orifices (not shown).

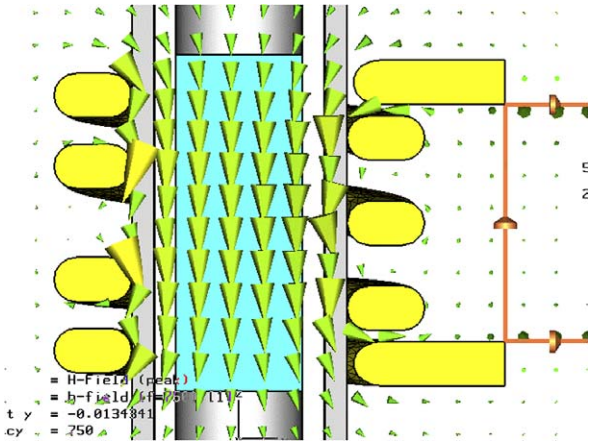

Fig. 2. **H**-vector plot, *XZ* plane, for coil #1 at 750 MHz. Although the *B* field is more commonly reported in the NMR literature, the *H* field is more readily available in standard software. In non-magnetic materials these fields simply differ by a constant factor, as $\mathbf{B} = \mu_0\mathbf{H}$. The cylindrical axis of the coil is denoted the *z*-axis in all plots.

$$Q_C \cong 1.3E07 C_P^{-0.85} f_0^{-1.35}, \quad (6)$$

where C_P is the capacitor value in pF and f_0 is the frequency in MHz. (The above expression gives values somewhat higher than the manufacturer's specifications but is a better fit to our data.) In all the simulations, the tuned coil is excited with a broadband Gaussian pulse source, 14.14 V peak, 50 Ω, centered very near resonance, which delivers 0.5 W to the coil when matched to 50 Ω. Also, the coils are inside a copper box, and both shield and radiation losses are negligible.

The magnitude plot in Fig. 3 gives a more precise perspective on the true B_1 field. This is a contour map of the component in the plane transverse to B_0 when the coil is at the magic angle. For the B_0 field axis in the XZ plane of the coil, it is obtained from $\sqrt{B_Y^2 + (B_X \cos\theta + B_Z \sin\theta)^2}$, where θ is the magic angle (~54.7°) and these unprimed field components are calculated in the spinner reference frame. (The most significant differences that would be seen between this plot and one of total H magnitude would be found near the ends of the sample and especially outside the coil.) Here, at 720 MHz, for a 50 mM saline sample ($\sigma = 0.58$ S/m and $\varepsilon_r = 77$), 11 mm length, the simulations gave a matched Q_L of 50.1 compared to the measured value of 46.5 for the same conditions. The simulated central H-field magnitude, at 0.5 W excitation, is 261 A/m, corresponding to a B field of 3.27 G. To get the correct transverse value in the rotating frame, this must be multiplied by 0.5 to correct for linear polarization and by Sin(54.7°) since the coil is oriented at the magic angle. Hence, the simulated central B_1 at 0.5 W is 1.34 G, or 5.7 kHz for protons.

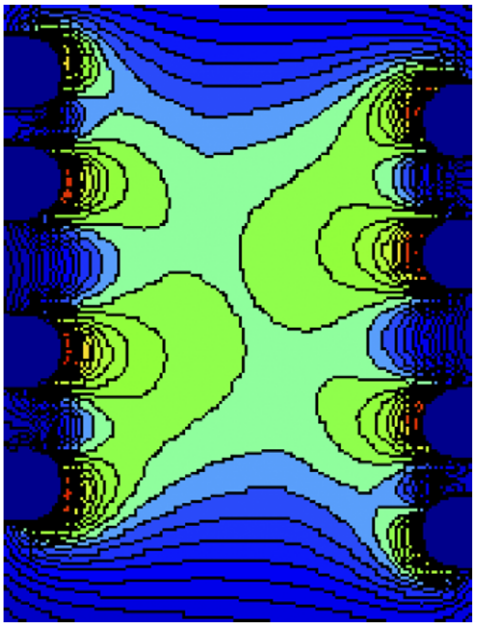

Fig. 3. YZ plane magnitude plot of the B_1 transverse component for coil #1 with the spinner axis at the magic angle. Contours are plotted from 200 to 300 A/m in increments of 3.3 A/m with a central value of 261 A/m.

By previous methods, the mean B_1 throughout the homogeneous length for a small solenoid is given by the following equation in mixed units [6]:

$$B_1 = \beta \left[\frac{PQ_T}{fV_C}\right]^{1/2}, \quad (7)$$

where β is a dimensionless function of coil geometry (in this case, estimating from [7], $\beta = 2.5$), f is in MHz, and V_C is the coil volume in mL. Hence, one would expect this coil at the magic angle to generate an effective mean field of 1.29 G at 0.5 W for $Q_T = 93$, in excellent agreement with the simulations.

The **E**-vector plot of Fig. 4 may surprise many readers. The fields within the sample are much smaller than the external fields because of the relatively high dielectric constant of the sample, and they are axially directed because they are dominated by the potential across the coil (i.e., second term in Eq. (3)) rather than dB/dt. It may also come as a surprise to see in the contour plot of Fig. 5 that the E

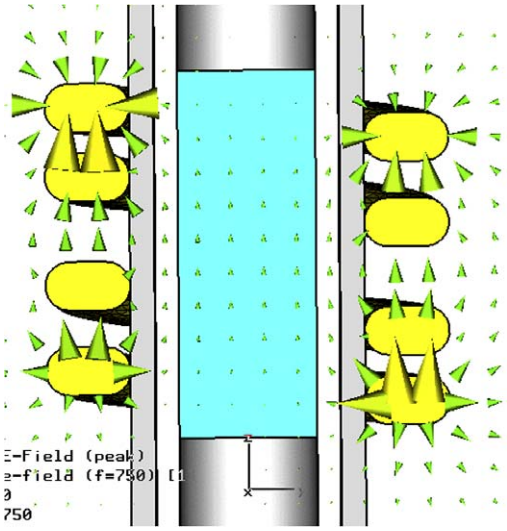

Fig. 4. E-vector plot, YZ plane, for coil #1 at 750 MHz.

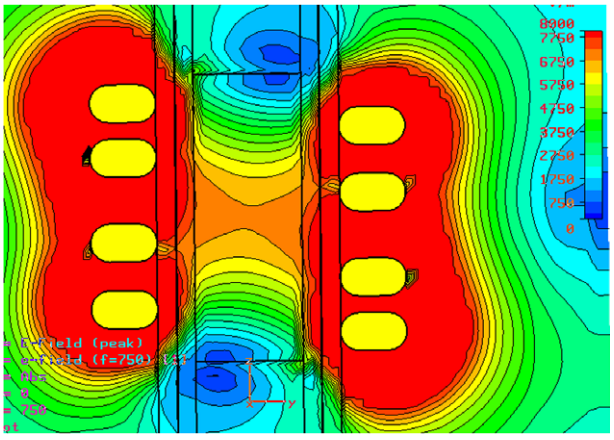

Fig. 5. E-magnitude plot, XZ plane for coil #1 at 750 MHz. The contours are at 17 equally spaced levels from 0 to 8000 V/m.

magnitude within the sample is greatest near the center and decreases rapidly at the ends—the opposite of what is happening between the turns. The central value is 6.8 V/mm, which is over an order of magnitude below the peak value occurring between the turns but still results in sample losses being large compared to coil and capacitor losses. Relative sample losses are proportional to $(\sigma E/B_1)^2$. Here, the mean $E/B_1 = 3.2$ V/mmG, and approximately 81% of the power is dissipated in the sample, 13.5% in the capacitors, and 5.5% in the coil. As the sample or rotor permittivity decreases, E/B_1 increases slowly, though the dependence is quite complex.

Note that since the coil voltage for a given B_1 in a given coil is simply proportional to frequency (from Faraday's law, $n\mathrm{d}\Phi_B/\mathrm{d}t$, where Φ_B is the magnetic flux in the coil), the axial electric field in the sample is also simply proportional to frequency for wire lengths small compared to lambda. Hence, from Eq. (1), the losses are essentially proportional to f^2, as σ increases by only 10% in typical tissues as f increases from 300 to 900 MHz [8].

Placing the solenoid on the inside of the coilform, as shown in Fig. 6, substantially improves performance with lossy samples, though there is less effect with low-loss samples and RF homogeneity may be degraded a little. Sample RF heating may be reduced by a factor of 2 to 4, depending on details of the spinner assembly. For the case simulated here (56.5 μL, 45 mM sample, 8 mm length, and 750 MHz), with a zirconia stator as pictured, the simulated **H** field was 295 A/m, mean $E/B_1 = 1.91$ V/mmG, capacitor losses are 16%, coil losses are 12%, and sample losses are 72%. Clearly, the reduction in E/B_1 within the sample is much greater than can be explained by just the reduction in the coil's inductance. The radial air gap (in this case, 0.4 mm) between the coil and the outer zirconia stator is found to be even more significant in affecting electric potential in the gas bearings—and hence electric field within the sample.

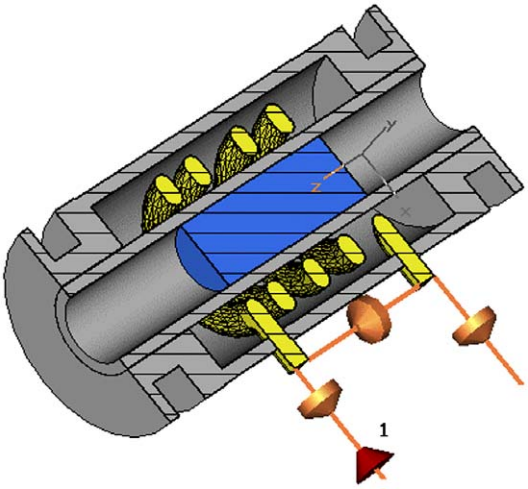

Fig. 6. Coil #2, the 4-turn solenoid inside the ceramic MAS stator, very close to the rotor.

2.4. The scroll coil

The loop-gap resonator (LGR, originally known as a split-ring resonator) has been widely used for two decades in electron paramagnetic resonance (EPR) because of its effectiveness in minimizing the electric fields within the sample region [9,10]. Being essentially a single-turn solenoid with an integral, distributed capacitor, the axial component of the electric field is eliminated, leaving the much smaller transverse components. This makes it an ideal coil for many single-tuned, high-frequency applications.

While the inductance of the LGR is too low for efficient triple-resonance applications, the similar multi-turn "scroll" coils, or multi-layer solenoids, also have very low electric fields (largely because the inner turn shields the E field from the outer turns) and have sufficient inductance for multiple tuning [10–12]. However, they have lower self-resonant frequency and reduced S/N—typically 37–45% lower for the 3.2 mm rotor at 500 MHz [11,13]. The reduced LF S/N arises from a combination of effects: (1) the currents are highly concentrated at the edges (leading to greatly improved B_1 homogeneity but reduced Q), (2) the outer layer needs to be at a rather large diameter for acceptable HF tuning, which reduces filling factor, and (3) the low inductance leads to inefficient multiple tuning. This coil has thus far seen only occasional use in NMR over the past two decades, partly because of its inferior S/N in high-field applications and partly because of its large temperature-dependent tuning shifts (from its large inter-layer capacitance and from its poor dimensional stability). It also appears to present greater challenges in achieving competitive B_0 homogeneity [13].

Fig. 7 shows the E field for a balanced 2-turn scroll coil, coil #3, on the outside of a 5.1 mm stator with the same

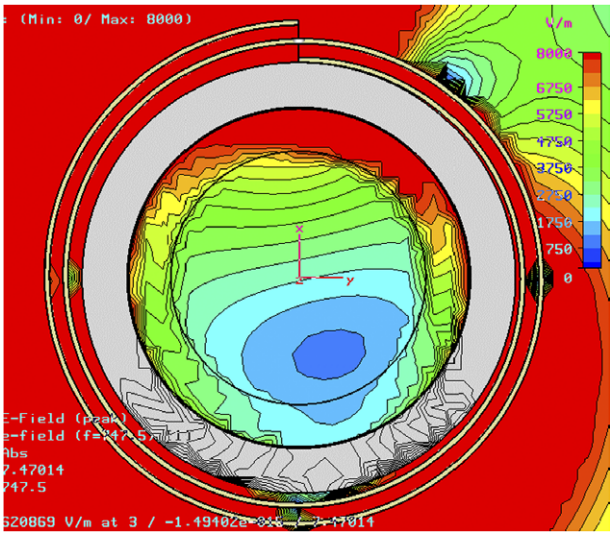

Fig. 7. E-magnitude plot, XY plane at $z = 2$ mm for a balanced 5 mm scroll coil, coil #3, at 750 MHz. Same range as Fig. 5. The asymmetry inside can be understood as due to the electric potential difference across the gap. Outside it depends on that plus the coil balance.

56.5 μL, 45 mM sample. With 0.5 W applied to this coil, the simulated H-field is 279 A/m, mean $E/B_1 = 0.87$ V/mmG, capacitor losses are negligible and coil losses are 60%. Relative RF heating is 20% that of coil #2. Here, a teflon dielectric thickness of 0.18 mm was used to obtain resonance near 750 MHz with zero external tune capacitance and 0.35 pF for match and balance. For comparison, the 3-turn scroll coil (with 5.1 mm ID) required a dielectric thickness of nearly 1 mm to resonate near 750 MHz, which led to an E/B_1 of 1.86 V/mmG. Operation above self resonance is possible by the addition of external tuning inductors, but efficiency suffers.

2.5. The optimized cross-coil

The Alderman-Grant coil has long been known to dramatically reduce the E/B_1 ratio within the sample, partly because voltage builds up only over half of the inductance of a similar one-turn saddle coil before it gets reversed by a segmenting capacitor, and partly because of the quadrupolar symmetry of the **E** field (the dipolar **E** fields at the two ends are oppositely directed). However, its B_1 homogeneity, as shown in Fig. 8, is relatively poor. A number of alternative ways of improving the B_1 homogeneity (and transverse flux transparency, magnetic filling factor, and Q) in coils of similarly low (or lower) relative electric fields, using parallel routes with insulated cross-overs, have been described elsewhere [14]. Also, we previously presented preliminary progress in improving the homogeneity of a design more suitable for small MAS coils by inserting an inner loop across the capacitors at one end, as shown laid out flat in Fig. 9 and in perspective view in Fig. 10 [2]. The relative current in the inner loop of this "XC" cross coil is controlled by the ratio of capacitance at the end where the inner loop is connected to that at the opposite end. The simulations show the optimum capacitance ratio is close to 1.35 for best homogeneity and filling factor with our current patterns when a magnetically orthogonal outer solenoid is also present, as shown in Fig. 11. The outer segmented bands still carry most of the current and are segmented (similar to the Alderman-Grant coil), and the small inner loops are driven at about half the voltage that would be present in a conventional one-turn saddle coil. (Our early attempts at putting a foil solenoid on the inside with a ^{1}H foil XC on the outside showed no S/N advantage for the solenoid and considerable degradation in the XC performance compared to the arrangement shown here. This is largely because putting the solenoid on the outside allows it to be made of heavy wire, which is advantageous in reducing lead losses and losses from current concentrations on the outside edges of the end turns, where losses in a foil solenoid are more concentrated. Other factors weighing against having the solenoid on the inside include dealing with the high voltage on the solenoid leads and the increased difficulties in getting satisfactory isolation and homogeneity at the HF.)

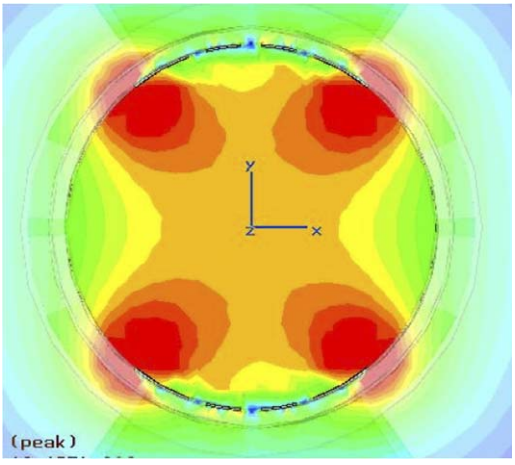

Fig. 8. H-magnitude plot, $z = 0$ plane, for an Alderman-Grant coil. The contours range from 100 to 400 A/m.

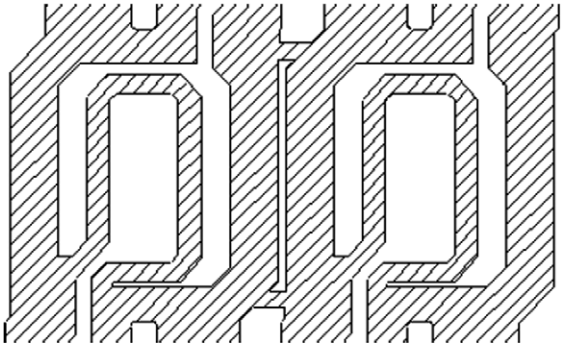

Fig. 9. Approximate foil pattern for the optimized cross coil.

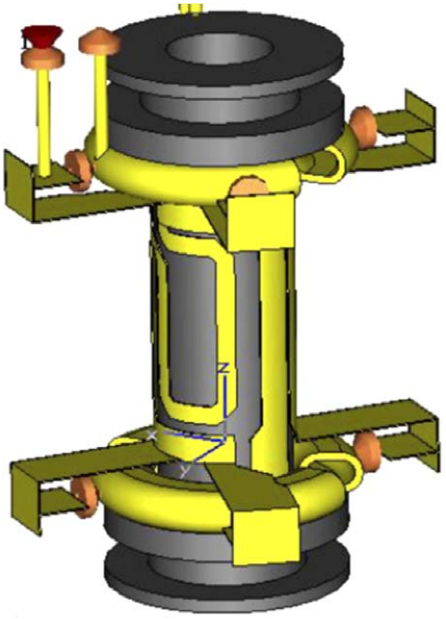

Fig. 10. The XC ^{1}H cross-coil on the ceramic stator, as simulated. Four chip capacitors, mounted on tubular buses, are used at each end for tuning, and two more are used for match and balance.

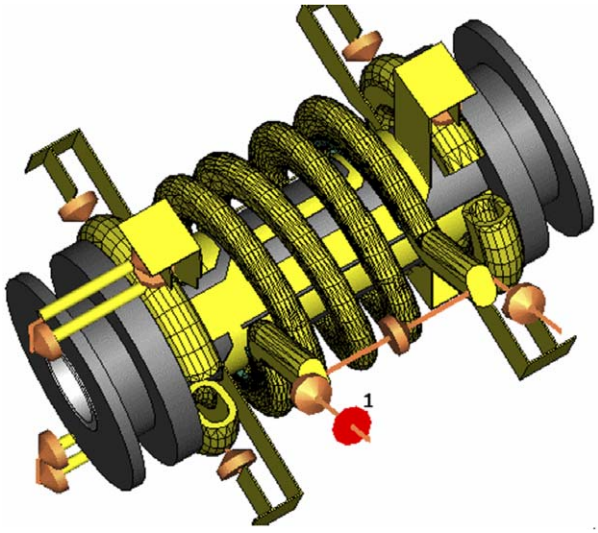

Fig. 11. The multi-nuclear solenoid coil is wrapped over the ^{1}H XC with 0.5 mm teflon insulation (not shown) between.

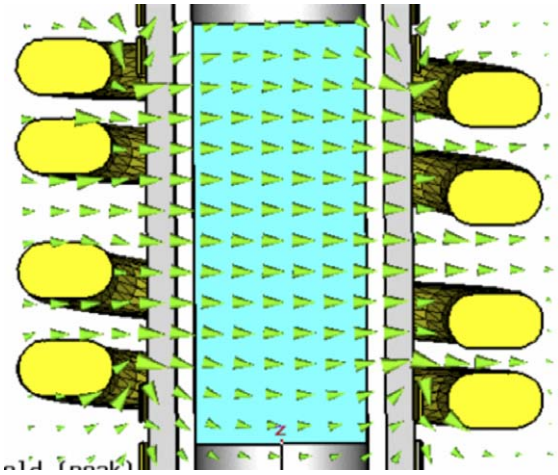

Fig. 12. **H** vector plot, *YZ* plane, for the XC coil of Fig. 11.

Simulations were performed with the 4mm Cross-coil (XC4) tuned to 750 MHz and driven with 0.5 W while the outer solenoid, which is used for multinuclear tuning to the MF and LF frequencies, had its leads shorted. Some results for the same 56.5 μL sample are shown in the next four figures. Fig. 12 shows an **H** vector plot in the *YZ* plane when the coil is aligned such that B_0 lies in the *XZ* plane. The B_1 homogeneity is shown more clearly by the true B_1 (component transverse to B_0) contour plots in Fig. 13 for the *YZ* and *XY* planes with the spinner at magic angle. With a sample with $\sigma = 0.5$ S/m, the simulated central *H*-field magnitude is 248 A/m, mean $E/B_1 = 0.67$ V/mmG, capacitor losses are 56% and coil losses are 35%. The B_1 field in the central region at 0.5 W is 1.7 G with a 2 mM saline sample, 1.55 G with a 45 mM sample, and 1.3 G with a 150 mM sample. Note that this field is transverse, irrespective of the spinner orientation; and sample heating, proportional to $(E/B_1)^2$, is an order of magnitude below that of coil #2. Also note that heating vanishes at the center, as seen from the *E*-field for the $y = 0$ plane in Fig. 14.

2.6. Calculating the sample temperature rise

As we are now able to accurately determine the **E** field using commercial software, it is possible to estimate the maximum temperature rise and gradients. For the case of heating being deposited uniformly throughout a long solid cylindrical sample of radius r_i, integration of the radial heat conduction (with power deposited according to Eq. (1)) for the case of uniform E, σ, and thermal conductivity k, and with length h, yields the following for the radial increase in temperature T_{RS} from the sample surface to the axis:

$$T_{RS} = \frac{\sigma E^2 r_i^2}{8k} = \frac{P_S}{4\pi hk}. \tag{8}$$

For the solenoid case, where E is larger near the axial center, the second expression in Eq. (8) underestimates T_{RS} at

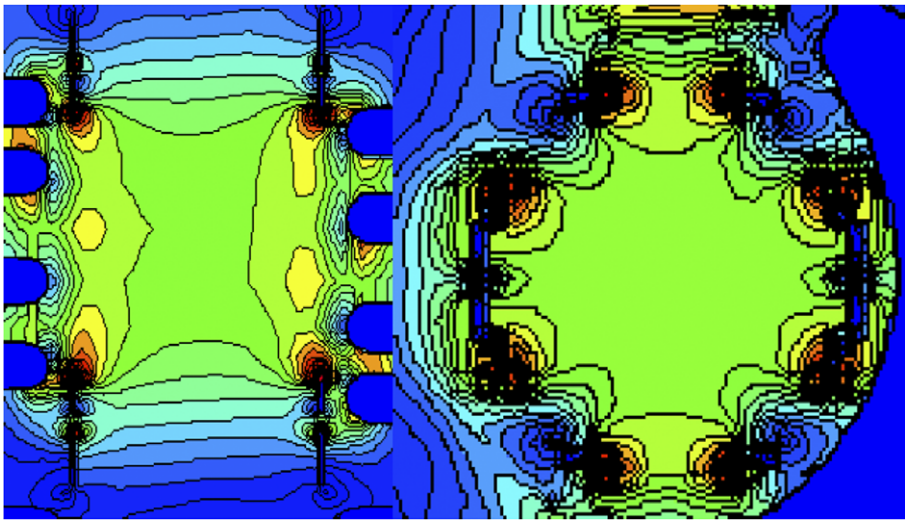

Fig. 13. Plots of B_1 in the *YZ* and *XY* planes, 200–300 A/m, 3.3 A/m per contour, of the component transverse to B_0 when the spinner is at the magic angle for the XC with a saline sample at 750 MHz. The outer solenoid is not driven at the high frequency.

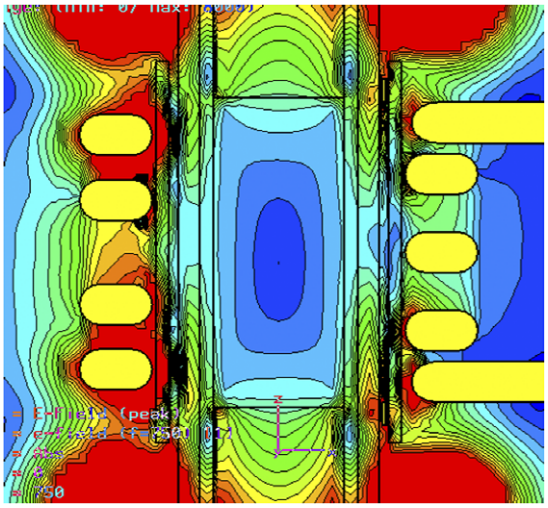

Fig. 14. Plot of the E magnitude from the XC at 750 MHz in the $y = 0$ plane (same scale as used in Fig. 5).

the center. It is useful to note that, in typical solenoid practice, E/B_1 increases at least linearly (usually faster) with the sample coil radius. Hence, T_{RS} typically increases at least as the fourth power of coil diameter and as the square of the frequency.

Note that Eq. (8) estimated the radial temperature rise only within the sample. This heat must then be conducted through the ceramic rotor of outer radius r_o. For a long coaxial tube of conductivity k_R and length h_R, with inner isothermal surface temperature T_i and outer isothermal surface temperature T_o, in the absence of heating within the tube wall, the temperature difference T_R between these surfaces arising from heat P conducted radially through the tube is given by the following familiar equation:

$$T_R = \frac{P \ln(r_0/r_i)}{2\pi h_R k_R}. \tag{9}$$

For a zirconia rotor, this T_R is typically about one-tenth of T_{RS}. However, a more significant axial gradient may be present, as the external cooling of the rotor surface near the center may be quite limited—except perhaps in designs where high velocity VT air flows directly over the middle of the rotor. The axial gradient is a complex function of numerous variables, including the rotor surface speed, air flow over the rotor surface, and the distance between the rotor surface and stator. In our case, a useful estimate of the axial temperature difference T_A from the center to the ends of the sample for a 4 mm zirconia rotor of thermal conductivity k_R at moderate spinning speeds (3–5 kHz), where k_R is large compared to k, was found to be

$$T_A \cong \frac{P_S h}{25 r_o^2 k_R}. \tag{10}$$

Also, in our case, the temperature increase on the rotor surface relative to the bearing gas temperature near the ends of the sample was approximately $0.5T_A$. Both estimates are consistent with about half of the deposited power being conducted axially away from the sample toward the gas bearings near the ends of the rotor. Hence, the total maximum sample temperature increase (center) is approximately $(1.1T_{RS} + 1.5T_A)$, and the minimum temperature rise (end edges) is about $(0.1T_{RS} + T_A)$.

2.7. Experimental tests of solenoid heating calculations

The upper trace in Fig. 15 shows the results of an experiment in which a solenoid, as shown in Fig. 1, was double tuned to 750 and 300 MHz, while the lower trace shows a similar experiment with the XC as discussed shortly. For the solenoid experiment, approximately 1.2 W was deposited continuously into the sample at 750 MHz (corresponding to an RF amplitude of 12 kHz for a 50 mM sample) while the temperature was monitored via the NMR chemical shift of ethylene glycol, $(CH_2OH)_2$, in a 7 T magnet. In this case, the fraction of incident 750 MHz RF power deposited in the sample was determined using Eq. (5), as the sample loading was substantial and good accuracy could be obtained by that method. The maximum equilibrium temperature increase of about 100 °C seen in the spectrum agrees within 10% with the above analysis for the effective axial E-field length of about 7 mm, as seen in Fig. 5, and the minimum temperature rise of 25 °C also agrees well with the above analysis. The dominant thermal time constant seen in the experiment was approximately 16 s. (For ethylene glycol at 350 K, $k \cong 0.26$ W/m-K and $\varepsilon_r = 31$; and for the zirconia rotor, $k = 3$ W/m-K.) Note the very large thermal gradient, about which we'll have more to say later.

Experiments were also performed in a triple-resonance 3.2 mm Varian MAS T3 probe at 700 MHz. Here, the rotor ID was 2.0 mm and the sample length was 6.6 mm, giving a sample volume of 20 μL, and the RF coil is on the inside of the coilform, similar to the geometry shown in Fig. 6. This probe was found to generate a 6.6 μs ^{1}H π-pulse with 46 W at the probe port for a low-loss sample, which corresponds to 1.85 G at 0.5 W. Power measurements were performed using an Agilent precision RF pulse meter, E4416A, with sensor E9321A, calibrated within 2%.

Several 2D-type pulse experiments were used on the above 700 MHz probe in which an 83 kHz proton heating pulse (of up to 60 ms) was applied, following by a relaxation delay of a little more than 2 s, following by a 90° pulse, followed by 819 ms signal acquisition. The total cycle time was kept fixed at 3000 ms, and 100 dummy scans were applied to establish thermal steady state before the spectrum was recorded. For a 60 ms heating pulse (2% duty cycle), the temperature rise, as indicated from the chemical shift, was 18 °C for 50 mM saline in methanol, which has $\varepsilon_r = 31$ at 310 K and conductivity of 0.53 S/m at 750 MHz [15]. The power applied at the probe port to achieve the 83 kHz field was 55 W, and the pulse power deposited in the sample was estimated to be 17.5 ± 3 W [16], implying ~38% of the ^{1}H power is delivered to the sample and sample coil. From Eqs. (8)–(10), the expected

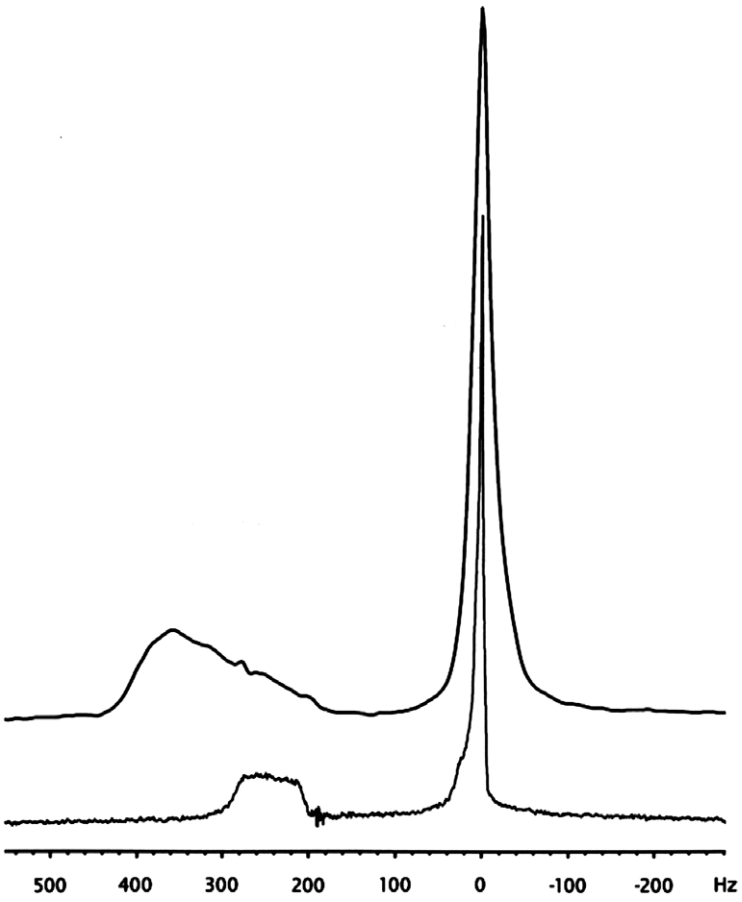

Fig. 15. Heating effect on the spectrum of ethylene glycol at 7 T for cw power deposited into the sample at 750 MHz. In the upper trace, 1.2 W is deposited by the solenoid case shown in Fig. 5. In the lower trace, 1.1 W is deposited by the XC case shown in Fig. 11.

mean temperature rise then would be ~26 °C (the homogeneous length is just a few percent less than the 4 mm case, but the thermal conductivity of the methanol is about 22% less than that of ethylene glycol). Note that the sample was spinning at only 2 kHz, so frictional heating, which is quadratic with spinning surface speed, was negligible. (Separately, mean frictional heating was found to be 17 °C at 18 kHz for this 3.2 mm spinner with a zirconia rotor. It was nearly twice as large in the XC4 probe for the same surface speed with a silicon nitride rotor and stator, owing to the differences in VT gas flow and the thermal conductivities of the rotor and stator materials.)

At steady state, the mean sample temperature is calculated to increase about 7 °C during each 60 ms 17 W pulse (using methods similar to those discussed later) and to cool 7 °C during the 2.94 s prior to the next pulse. The acquisition begins 2.06 s after the heating pulse and the FID is largely decayed within 100 ms, so the sample temperature is being measured ~2.1 s after the heating pulse, at which point it will be 1.4 °C below its mean value. Hence, the expected sample heating in the NMR experiment would be ~25 °C for a 3.2 mm stator design similar to that of the XC4. The NMR experimental value of 18 °C in the Varian probe suggests its central rotor cooling method reduces its axial thermal gradient for a given amount of RF heating. It should also be noted that the pulse heating calculation assumed uniform heating throughout the sample and the immediately adjacent materials. A more detailed picture would probably show central peak heating of ~15 °C at the end of the pulse, rapidly equalizing to ~5 °C within ~0.5 s after the pulse.

3. Results and discussion

3.1. XC4 experimental results

Careful RF power and pulse length measurements were carried out for the low-loss, low-dielectric case on the triple-resonance XC4 probe at 750 MHz, again using the Agilent E4416A pulse power meter. For pulse power of 46 W (measured at the probe port), the pw180 was 9.24 μs. Linear RF circuit simulations (using ARRL Radio Designer, a node-list-based simulator similar to the widely used PSPICE) suggested the power losses in the matching circuit (leads, quartz variables, balancing coils, transmission line in probe) totaled ~20%. With that assumption, the NMR-measured pw180 should be 81 μs for 0.5 W at the coil, corresponding to a γB_1 of 6.2 kHz, or a mean field of 1.45 G. The simulations give 1.7 G for the central value. The 15% difference is mostly the difference between the

mean over the sample (in the NMR experiment) and the central maximum (in the simulations). Similar agreement was inferred for the saline samples on the basis of relative circuit Q. The coil withstood 30 ms pulses up to 250 W, corresponding to 125 kHz and the limit of the power amplifier.

The accuracy of the RF absorption from the CST MWS simulations was validated by monitoring the rate of rise of the sample temperature (from the ethylene glycol chemical shift) at several different 750 MHz irradiation levels (recall from Fig. 15, in a 7 T field)—here using a silicon nitride rotor and 150 mM salinity. The sample mass was 66 mg with $C_P = 2414$ J/kg K and the rotor mass in the sample region (and ~4 mm beyond each end) was 200 mg with $C_P = 740$ J/kg K. The reciprocal of the sum of mC_P for the sample and affected rotor is 3.26 K/sW. The thermal time constant for heating within this region was short compared to the time constant of the heating experiments (21 s at 4.4 W continuous RF input), allowing most of the thermal mass of the rotor and some of the end caps to be included with that of the sample. (For examples: for the rotor in direct contact with the sample the thermal time constant was calculated to be 0.01 s; the time constant for radial conduction within the plastic caps was ~16 s, and that for axial conduction to the ends of the rotor was similar.) At 4.4 W input RF power, the initial rate of rise in the sample was 2.6 K/s, and at 7.6 W the initial rate of rise in the sample was 4.2 K/s, giving an average of 0.58 K/J, or 18% of the above calculated heating rate. Hence, about 18% of the ^{1}H RF power at the probe port was deposited into the sample. (The initial rate of rise was determined from a single exponential fit to the heating data during the first seven seconds plus the final equilibrium temperature, which was 37 °C above ambient for the case of 4.4 W at the probe port.)

As noted earlier, the circuit simulations indicated 80% of the ^{1}H RF power was delivered to the XC coil, chip capacitors, and sample. The CST simulations indicated 19% of that power (i.e., 15% of the port power) was deposited in the sample. Further experiments at 62 MHz, where internal sample heating was negligible, suggested about 13% of the RF power dissipated in the coil and chip capacitors would be conducted into the sample with a time constant of about 50 s at a spinning rate of 4 kHz, so this direct coil heating may have increased the sample temperature ~2% in the 750 MHz 7-s heating experiment. Hence, the CST power absorption results agreed quite well with these NMR experiments for the XC4 at 750 MHz.

Since, the E field in the XC vanishes in the center, much lower thermal gradients are expected from it than from the solenoid when total power absorptions are similar (compare Figs. 5 and 14). This is partially illustrated by the reduced broadening in the lower trace in Fig. 15 compared to the upper trace, where the total powers deposited in the samples are about the same (though B_1 is about 4 times greater for the XC for the same sample). However, both spectra were acquired after irradiation times very long compared to thermal time constants within the sample. The relative advantage of the XC compared to the solenoid in thermal gradients should be much greater during 50 ms decoupling pulses, for example.

Table 1 summarizes much of the preceding material for several representative 4 mm cases at 750 MHz for balanced single-tuned solenoids at the magic angle and for the ^{1}H XC with an outer solenoid for MF and LF tuning with sample relative permittivity of 80 and a zirconia rotor. Note that the B_1 and pw180 values correspond to the center of the sample, not the mean throughout the sample.

3.2. Triple-tuning the single solenoid

The solenoid simulations thus far have been for balanced single-tuned coils, but more often triple-resonance capability is required. For the XC with solenoid, the HF losses associated with the LF/MF solenoid are minor and have already been included, but for the triple-tuned solenoid, the additional HF losses are quite substantial, especially for larger, low-loss samples. A number of circuits suitable for triple-tuned solenoids have been used [1,17–21], and a recent variant, similar in many respects to our earlier "Twin-line" circuit [18], is illustrated in Fig. 16 as an example, with a few brief comments. The sample solenoid is shown as two coils in series simply to make its center available for monitoring the voltage there (node 11) to verify coil balance in the simulations. Most of the transmissions lines (TRLs) are minimal-length leads, with the notable exception of TRL1, which is chosen to permit simple tuning of the HF. (The sum of the lengths of TRL1,

Table 1
Balanced, single-tuned, coil simulation data for 4 mm MAS at 750 MHz

	Units	Sol. #1	Sol. #2	Sol. #2	2-t Scroll	XC w.sol.	XC w.sol.
Sample cond.	S/m	0.02	0.02	0.5	0.5	0.02	0.5
pw180 @ 250 W	μs	2.52	2.66	3.48	1.85	3.1	3.38
B_1 @ 0.5 W	G	2.08	2.0	1.51	2.87	1.7	1.55
V_C @ 0.5 W	V	226	172	133	154	54	48.5
Mean E/B_1	V/mmG	3.2	1.9	1.91	0.87	0.67	0.67
B_1 inhomo., 56 μL	rms %	4	6	6	2	3	3
Q_L	—	98	73	47	259	130	87
Coil losses	%	23	19	12	60	42	35
Sample absorp.	%	23	21	72	40	2	9

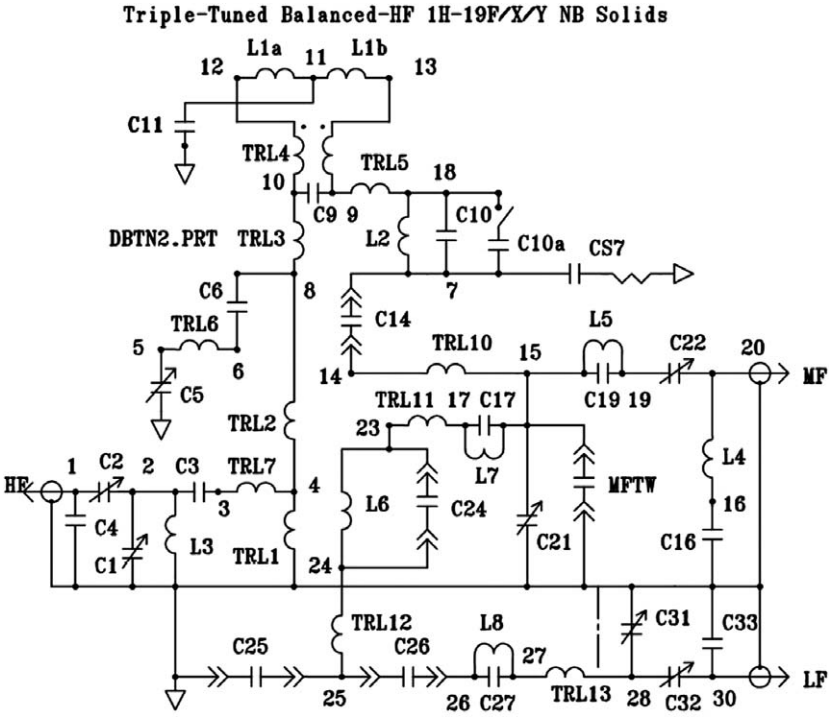

Fig. 16. A triple-tuned solids solenoid circuit with balanced HF.

TRL2, TRL3, and TRL4 is a little less than $\lambda/4$ at the HF.) HF balancing is essential to achieve HF field profiles similar to those at the MF and LF [22], as needed for efficient CP, and this is achieved with L2 and C10 (and with C10a for ^{19}F tuning). LF isolation to the MF port is established primarily by the choice of C14, and MF isolation to the LF port is established by resonance of L6 and C24. The circuit achieves the desired objectives of balancing the sample coil at the HF and matching to the coil at three frequencies about as efficiently as is generally practical. If necessary, the LF tune and match variables, C31 and C32, may be somewhat remote from the sample region, via TRL13, with little loss in performance.

Table 2 compares the efficiencies expected from circuit simulations (similar to some previously validated in a triple tuned 5 mm narrow bore (NB, also often called standard bore, SB) MAS probe at 600 MHz) for the circuit of Fig. 16 with a 4 mm rotor, a low-loss sample, and multinuclear tuning to those of an alternative circuit for a 2.5 mm rotor with fixed H/C/N tuning at 800 MHz [1]. The 2.5 mm probe was not significantly loaded by a saline sample [23], and it achieved higher efficiencies because (1) its sample coil was smaller (hence, its Q was lower), (2) its tuning was fixed, and (3) several of its specially fabricated capacitors had higher Q. In an earlier section, we saw that a 3.2 mm probe with a similar circuit achieved HF RF efficiency of about 38% with a 50 mM saline sample. The important point here is that the B_1 fields presented earlier for the balanced, single-tuned solenoid are of limited value in estimating the performance of a probe utilizing a triple-tuned solenoid.

Table 2
Predicted RF efficiencies of triple-tuned "single-coil" solids circuits at 800 MHz

Circuit	Sample vol.	Salinity	% RF efficiency		
	μL	mM	^{1}H	^{13}C	^{15}N
Martin/Zilm, 2.5 mm, fixed	6.5	0	40	44	40
Doty, 4 mm, multi-nuclear	50	0	21	16	28
Doty, 4 mm, multi-nuclear	50	150	84	29	30

Note that "RF efficiencies" in Table 2 are higher with the high salinity 4 mm sample because "RF efficiency" here is defined as the percentage of RF power dissipated in the sample coil and sample, and the sample loss increases rapidly with salinity. In single-tuned coil circuits, we define RF efficiency as the percentage of RF power dissipated in the sample, the sample coil, and its local tuning capacitors.

3.3. The double-tuned outer LF/MF solenoid

When an XC is used for the HF, all three channels may be more efficiently accommodated. The RF efficiency of the single-tuned XC (here we include power dissipated in its local capacitors) is approximately 80%, irrespective of the load, and LF and MF efficiencies are higher in an orthogonal outer solenoid than in a triple-tuned circuit. Fig. 17 illustrates a circuit we have often used for the double-tuned multi-nuclear solenoid, L1. Here, it is easier to achieve high efficiency and excellent isolation than in the circuit of Fig. 16. Also, by simply removing C7, it is easily converted to a balanced, single-tuned circuit. However, the biggest advantage of taking the HF out of the MF/LF circuit

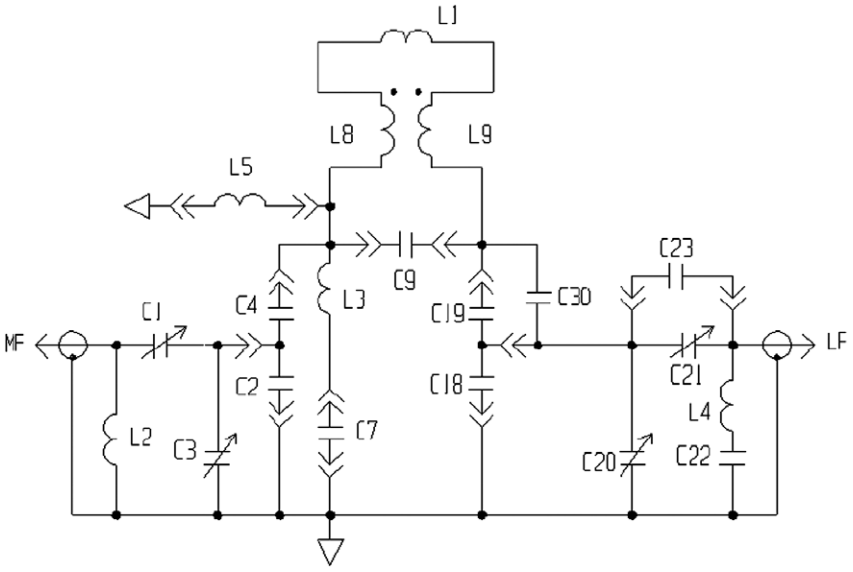

Fig. 17. A double-tuned multi-nuclear solids solenoid circuit.

may be that it permits the tuning of all three channels to be stable and efficient even with rather long leads (identified as L8 and L9 in Fig. 17), and this seems essential for the axis re-orientation needed to accommodate automatic sample ejection/loading in narrow-bore magnets. Also, we have recently shown that it permits switched angle spinning (SAS) in narrow bore magnets.

The outer solenoid is normally only slightly affected by the inner XC, even though RF eddy currents of fairly large magnitude, though of small extent, are induced in the XC, as portrayed in Fig. 18. The effect is to reduce the solenoid's unloaded Q and the magnetic filling factor, each by about 20%. Nevertheless, the corresponding magnetic field plots at the LF and MF are almost indistinguishable from those shown previously for the solenoid without the inner XC in Figs. 2 and 3. The electric field is greatly reduced and roughly constant throughout the sample region, as the XC acts as a Faraday shield for the solenoid. As a result, Q_L with very lossy samples is improved (for example, by 61% for a 150 mM 4 mm sample at 189 MHz), and RF sample heating is reduced, typically by a factor of 30, at all LF and MF frequencies.

It is important to insure that the RF field profiles at the different frequencies match rather closely, or CP effectiveness can be seriously degraded. As recently pointed out, this mismatch can be quite significant for an unbalanced multi-tuned solenoid in a 2.5 mm MAS probe at 800 MHz [22]. Fig. 19 shows calculated mean (average over a transverse slice) transverse field for the XC and axial field for the solenoid when the coils are properly aligned—the geometric center of the solenoid is shifted 0.5 mm from the center of the XC's inner loop toward its drive end.

While axial B_1 profiles of solenoids are useful, they are not always sufficient to explain or predict NMR results. In some cases, B_1 inhomogeneities transverse to the spinner axis can have significant effects [24]. Generally speaking, these inhomogeneities give rise to amplitude and phase modulations of B_1 (as well as of the detected NMR signal [25]) as a sample volume element orbits about the spinner axis. These modulations tend to be small, but as they are synchronous with the sample rotation, they can lead to unintended spin dynamics when the applied RF pulse sequence is also rotor-synchronous, as is the case for most recoupling sequences.

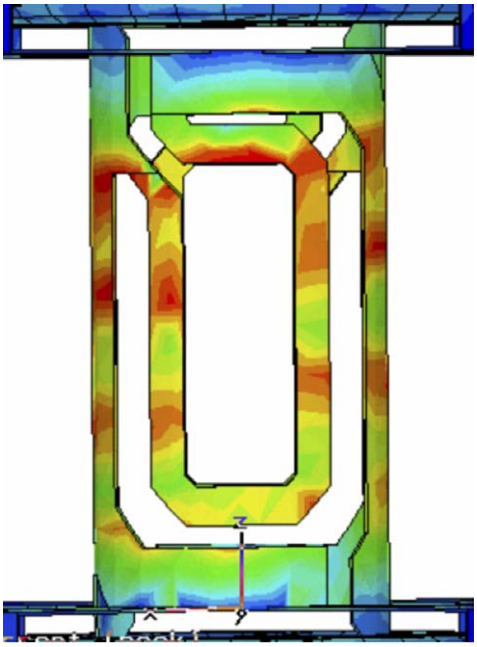

Fig. 18. Magnitude of surface current density induced in the XC by the outer solenoid at 189 MHz.

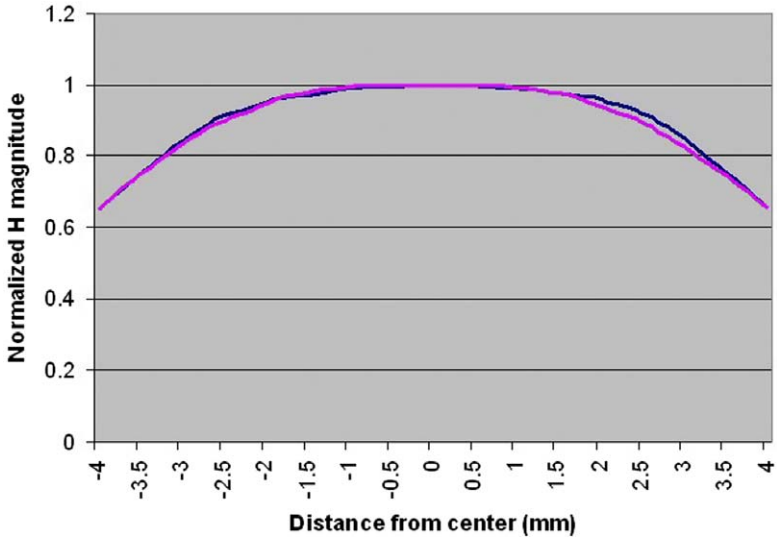

Fig. 19. Normalized mean B_1 fields as a function of the axial position, as simulated for the two coils with a 50 mM saline load with alignment as discussed in the text.

3.4. NMR XC4 test results

In the above experimental XC4 probe, the silicon nitride stator unfortunately had minor magnetic defects which added about 15 Hz to the proton line width. We measured S/N on glycine at 218:1 for ^{13}C in the H/C/N tuning configuration. The S/N was extracted computationally from the digital spectral data using a 1000 Hz noise region, adopting the standard commercial practice of defining the signal-to-noise ratio as the peak height divided by twice the root mean square noise.

The ^{13}C spectrum for natural-abundance glycine at 17.6 T taken with the 4-turn coil is shown in Fig. 20 for the H/C/N tuning configuration. Line broadening of 80 Hz was applied with a signal acquisition time of 30 ms. Even though this is a low-loss sample, the S/N in this multi-nuclear probe exceeds that reported for an alternative 4 mm H/C/N 750 MHz NB probe in the H/C tuning configuration by a substantial factor. Primary RF efficiency parameters and power handling of the completed probe are summarized in Table 3.

For reference, we note that for a given sample, the S/N for a single 90° pulse is indicated by the following:

$$\mathrm{S/N} \propto \left[\frac{\sqrt{T_2^*}}{T_S\sqrt{T_n + T_P}}\right](\eta_E \eta_f Q V_S)^{1/2}\omega^{3/2} \tag{11}$$

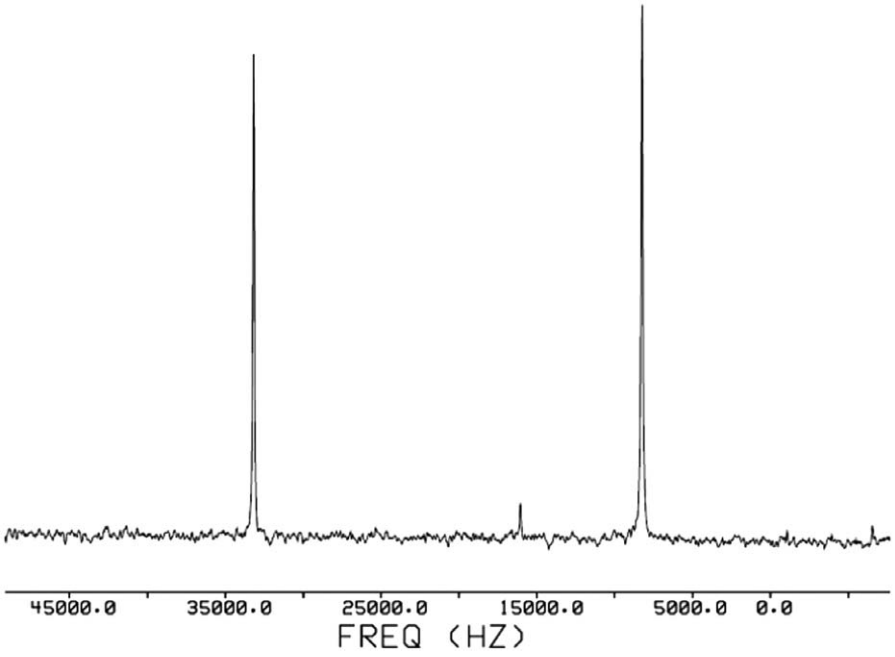

Fig. 20. Natural-abundance glycine ^{13}C with H/C/N tuning, 4 scans, 110 kHz TPPM ^{1}H decoupling, 70 μL sample, ramped-CP at 50 kHz for 1 ms, 17 kHz MAS. S/N = 218.

Table 3
Measured RF performance of XC4 MAS multi-nuclear probe at 750 MHz

	Units	2 mM sample			150 mM sample		
		^{1}H	^{13}C	^{15}N	^{1}H	^{13}C	^{15}N
RF efficiency	%	80	29	47	82	36	49
pw90	μs	2	5	7	2	5	7
Power	W	200	420	600	240	430	670
Q_L	—	120	103	86	101	100	77

where T_2* is the effective spin-spin relaxation time, T_S is the sample temperature, T_n is the weighted mean temperature of the lossy elements (coil, capacitors, and sample), T_P is the preamp noise temperature, η_E is the RF circuit efficiency, η_f is the coil's magnetic filling factor, V_S is the sample volume, and ω is the Larmor frequency [6]. For given NMR test conditions (sample, B_0, T_2^*, T_S,T_n, T_P, and method),

$$S/N \propto \frac{B_1 V_S}{\sqrt{P}}, \tag{12}$$

where P is the power required to generate B_1 [6]. The above, which is sometimes referred to as the principle of reciprocity, is useful in comparing the data in Table 3 to the technical performance of other probes. Of course, T_2^* often depends on decoupling field strength and sequence, coil susceptibility, spinning speed, sample preparation and packing technique, and possibly other factors, so one must also look at other probe characteristics.

We noticed the B_1 homogeneity of the solenoid was less than we were expecting, as the signal amplitude obtained with a 810° pulse was only 60% that of a 90° pulse for a 6.5 mm sample length, though the 810/90 amplitude ratio was ~89% for a 4 mm sample length. Simulations suggested a 5-turn coil should give about 10% better central B_1 homogeneity as well as some improvement in RF efficiency, so a 5-turn coil was evaluated. With the 5-turn coil, the 810/90 ratio was found to be 90% for a 4 mm sample length and 63% for the 6.5 mm sample length. However, the stator was too short to allow sufficient space to handle the desired coil voltages.

3.5. Other challenges

In addition to the primary emphasis of this paper, RF sample heating and RF efficiency, there are other characteristics of importance in modern solids probes—including Q stability under high-power pulses (for inverse experiments), B_0 homogeneity, phase transients, multi-nuclear tuning, reliability, and compatibility with fast sample spinning, magic angle gradient (MAG) coils, variable temperature operation, high RF power, high fields, and automatic sample exchange [26]. We comment here briefly on several of these issues. The XC is bonded to the ceramic stator to stabilize its temperature and hence Q. The external solenoid may be quite massive, being constrained only by a MAG coil, if present, and magnetic compensation accuracy. Care is required in the selection and placement of the chip capacitors to assure good B_0 homogeneity in an XC probe [2], but we currently routinely achieve 1.2 Hz ^{1}H linewidth in a 40 μL sample at 300 MHz and expect that similar resolution will soon become routine at 750 MHz. Phase transients have been found to be substantially smaller with the cross coil than in triple-tuned solenoid circuits, where much higher RF energy must build up in additional tanks external to the sample coil before the impedance, phase, and amplitude stabilize. The approach presented herein has recently been shown to be suitable for use in a multi-nuclear, triple-resonance, NB MAS probe at 930 MHz [27]. The reduced effect of lead lengths from the use of two coils, separately optimized for their respective frequencies, has also been shown to be beneficial when axis re-orientation is desired [26], as for automatic sample exchange in narrow-bore magnets. Other recent advances, especially increased power handling, improved spinning technology, and high-performance MAG coils, will be reported in the near future.

4. Conclusion

We have shown that, assuming adequately refined meshes, an extremely reliable assessment of NMR RF coil performance may be obtained from a commercially available software package, CST MWS 5.1, with regards to the E and B fields as well as coil L, Q, and mode frequencies, both loaded and unloaded. From the ratio of E/B, we have seen that placing a solenoid inside the MAS stator often reduces sample heating by more than a factor of two compared to having it on the outside of the stator. The scroll coil provides a further reduction in heating of about a factor of five along with a significant improvement in B_1 homogeneity, but it suffers from typically a 40% loss in S/N and apparently other serious challenges in B_0 homogeneity and tuning stability. The use of the optimized cross coil for the ^{1}H, with the LF and MF on an outer solenoid, permits another factor of two reduction in decoupler heating compared to the scroll coil, with no penalty in S/N, B_1 homogeneity, or tuning robustness compared to the solenoid, at least above ~12 T, though at lower fields with small samples, the two-coil approach has slightly inferior S/N for low-loss samples. Sample heating is also very effectively addressed from the use of small rotors, as RF heating scales at least as the fourth power of the rotor diameter and as the square of the frequency; and directly blowing VT air on the central portion of the rotor may reduce sample thermal gradients by 30% for a given amount of RF heating. While there is some increased complexity in the XC coil technology, it affords substantial advantages at high fields in S/N for lossy samples requiring high-power decoupling.

Acknowledgments

This work was supported by NIH R43 RR018423-01 and NIH EB002026. The assistance of Siddarth Shevgoor

and John Staab, both of Doty Scientific, with some of the time-dependent thermal and RF calculations is also gratefully acknowledged.

References

[1] R.W. Martin, E.K. Paulson, K.W. Zilm, Design of a triple resonance MAS probe for high field solid-state NMR, Rev. Sci. Instrum. 74 (2003) 3045–3061.

[2] F.D. Doty, Y.A. Yang, G.E. Entzminger, Magnetism in NMR probe design part II: HR MAS, Concept Magn. Reson. 10 (1998) 239–260.

[3] F.D. Doty, G. Entzminger, C. Hauck, J.P. Staab, Practical aspects of birdcage coils, J. Magn. Reson. 138 (1999) 144–154.

[4] J. Tropp, Image brightening in samples of high dielectric constant, J. Magn. Reson. 167 (2004) 12–24.

[5] T. Weiland, Time domain electromagnetic field computation with finite difference methods, Int. J. Num. Mod. 9 (1996) 295–319. Also, see http://www.cst.de.

[6] F.D. Doty, Probe design and construction, Encyclopedia of Nuclear Magnetic Resonance, Wiley, New York, 1996, pp. 3753–3762.

[7] F.D. Doty, R.R. Inners, P.D. Ellis, A multinuclear double-tuned probe for applications with solids or liquids utilizing lumped tuning elements, J. Magn. Reson. 43 (1981) 399–416.

[8] D.L. Means, K.W. Chan, Evaluating compliance with FCC guidelines for human exposure to RF EM Fields, FCC OET Publication 65, supplement C (2001). http://www.fcc.gov/Bureaus/Engineering_Technology/Documents/bulletins/oet65/oet65c.pdf. Note that ε'' in pure water is essentially proportional to frequency between 10 MHz and 5 GHz, which means dielectric loss in pure water increases with the cube of the frequency, in contrast to the quadratic dependence for typical saline solutions.

[9] W.N. Hardy, L.A. Whitehead, Split-ring resonator for use in magnetic resonance from 200–2000 MHz, Rev. Sci. Instrum. 52 (1981) 213–216.

[10] F.D. Doty, Resonator sensitivity optimization in magnetic resonance and the development of a magic angle spinning probe for the NMR study of rare spin nuclei on catalytic surfaces, Ph.D Dissertation, University of South Carolina, Columbia, SC, 1983;
F.H. Larsen, P. Daugaard, H.J. Jacobsen, N.C. Nielsen, Improving RF field homogeneity in solid-state MAS NMR using a loop-gap resonator, J. Magn. Reson. A 115 (1995) 283–286.

[11] J.A. Stringer, C.E. Bronnimann, C.G. Mullen, D.H. Zhou, S.A. Stellfox, Y. Li, E.H. Williams, C.M. Rienstra, Reduction of RF-induced sample heating with a scroll coil resonator structure for solid-state NMR probes, J. Magn. Reson. 173 (2005) 40–48.

[12] S.C. Grant, L.A. Murphy, R.L. Magin, G. Friedman, Analysis of multilayer RF micro-coils for NMR spectroscopy, IEEE Trans. Magn. 37 (2001) 2989–2998.

[13] W.T. Franks, D.T. Graesser, D.H. Zhou, B.J. Wylie, B.G. Money, M. Hudock, G. Sahota, C.M. Rienstra, Protein Structure Determination by MAS NMR. Presented at the 15th ISMAR, Ponte Vedra Beach, 2004.; J.A. Stringer, C. Mullen, C.E. Bronnimann, D.H. Zhou, S.A Stellfox, C.M. Rienstra, K. Mehr, E.H. Williams, Performance of a Multiply Tuned Scroll Coil Resonator in Solid State NMR Experiments. Presented at the 46th ENC, Providence, 2005.

[14] F.D. Doty, G. Entzminger Jr., C.D. Hauck, Error-tolerant RF litz coils for NMR/MRI, J. Magn. Reson. 140 (1999) 17–31.

[15] By comparing detailed MWS simulations and bench measurements of Q_L for solenoids as shown in Fig. 3, tuned between 720 and 780 MHz, we measured the following effective conductivities: 50 mM NaCl in methanol, 0.53 S/m; neat ethylene glycol, 0.46 S/m; 50 mM NaCl in ethylene glycol, 0.66 S/m; and 150 mM NaCl in ethylene glycol, 0.8 S/m.

[16] Simulations of the 4 mm case shown in Fig. 6 ($\sigma = 0.5$ S/m, $\varepsilon_r = 80$), predicted the power deposited in the 56 μL sample and coil at 83 kHz would be 60 and 10 W, respectively, corresponding to a mean temperature rise of ~62 °C at 2% duty cycle, as confirmed in Fig. 15. For the 3.2 mm rotor at 700 MHz, the sample volume is 36% of the 4 mm case, and E/B_1 is down by ~25% from the combination of frequency and coil geometry (reduced diameter, but five turns instead of four). The reduced sample permittivity increases E/B by ~15%. Hence, for 50 mM methanol, the sample power absorption in the 3.2 mm rotor should be ~29% of the 4 mm saline water case, or ~17.5 W.

[17] F.D. Doty, Triple-Resonance Single-Coil Circuits for Solids NMR Probes. Presented at the 33rd Rocky Mountain Conference on Analytical Chemistry, Denver, 1991;
F.D. Doty, Doubly Broadband Triple Resonance NMR Probe Circuit, U.S. Pat #5,424,645, 1995.

[18] Y.A. Yang, F.D. Doty, G. Entzminger, Twin-Line Triple-resonance Circuit for High-Field NMR MAS. Presented at the 36th ENC, Boston, 1995.

[19] J. Stringer, G. Drobny, Methods for the analysis and design of a solid state nuclear magnetic resonance probe, Rev. Sci. Instrum. 69 (9) (1998) 3384–3391.

[20] Q.W. Zhang, H. Zhang, K.V. Lakshmi, D.K. Lee, C.H. Bradley, R.J. Wittebort, Double and triple resonance circuits for high-frequency probes, J. Magn. Reson. 132 (1998) 167–171.

[21] N. Sinha, C. Grant, C. Wu, A. De Angelis, S. Howell, S. Opella, SPINAL modulated decoupling in high field double- and triple-resonance solid-state NMR experiments on stationary samples, J. Magn. Reson. 177 (2005) 197–202.

[22] E.K. Paulson, R.W. Martin, K.W. Zilm, Cross-polarization, radio-frequency field homogeneity, and circuit balancing in high-field solid-state NMR probes, J. Magn. Reson. 171 (2004) 314–323.

[23] Kurt Zilm, Personal communication, 2004.

[24] K. Elbayed, B. Dillmann, J. Raya, M. Piotto, F. Engelke, Field modulation effects induced by sample spinning: application to high-resolution magic angle spinning NMR, J. Magn. Reson. 174 (2005) 2–26.

[25] P. Tekely, M. Goldman, Radial-field sidebands in MAS, J. Magn. Reson. 148 (2001) 135–141.

[26] F.D. Doty, J. Kulkarni, G. Entzminger, S. Shevgoor, R. Wells, K.P. Shevgoor, J.P. Staab, C. Xiao, J. Gravel, L.L. Holte, J. Shinohara, T. Bielecki, C. Turner, Comparisons of MAS Decoupler Heating of Samples by Various RF Coil Geometries at 750 MHz. Presented at the 44th ENC, Asilomar, 2004.

[27] K. Saito, Industrial Application of Multi Nuclear Solid State NMR at High Field (16.4 T) and Super High Field (21.8 T). Presented at the 47th ENC, Asilomar, 2006.